Preprint typeset in JINST style - HYPER VERSION

arXiv:0909.0242v1 [physics.ins-det] 1 Sep 2009

A comprehensive study of rate capability in Multi-Wire Proportional Chambers

A. Andronic[a], C. Garabatos[a],D. Gonzalez-Diaz[a]*, A. Kalweit[a], F. Uhlig[a]

[a] *GSI Helmoltzzentrum für Schwerionen Forschung, Darmstadt, Germany*
E-mail: D.Gonzalez-Diaz@gsi.de

ABSTRACT: Systematic measurements on the rate capability of thin MWPCs operated in Xenon, Argon and Neon mixtures using CO_2 as UV-quencher are presented. A good agreement between data and existing models has been found, allowing us to present the rate capability of MWPCs in a comprehensive way and ultimately connect it with the mobilities of the drifting ions.

KEYWORDS: CBM; TRD; rate capability; Xenon; Argon; Neon; CO_2; ion mobility.

*Corresponding author

Contents

1. Introduction **1**

2. Experimental setup and description of the measurements **2**

3. Gain curve measurements and chamber stability **5**

4. Rate capability measurements **8**
- 4.1 The Mathieson model 8
- 4.2 Extrapolation to infinite area of illumination 9
- 4.3 Fitting procedure 12
- 4.4 Calculations for minimum ionizing particles 16

5. Discussion **18**

6. Conclusions **20**

A. Results of the fit **21**

1. Introduction

Due to their good position resolution, low material budget and low cost, multi-wire proportional chambers (MWPCs) are instrumental in high-energy physics. They are currently employed in experiments needing high resolution tracking (ALICE-TPC [1]), muon spectrometers (LHCb [2]) and photo-sensitive detectors (HADES-RICH [3] or ALICE-TRD [4]), to mention some examples. In particular, a new generation of fast MWPC counters aimed at TR detection has been envisaged for the CBM experiment at FAIR [5]. The system's conceptual design (presented in [6]) is based on a configuration aiming at a pion suppression better than 100 for momenta higher than $p = 1.5$ GeV/c with position resolution of the order of 200-300 μm [7] at incident fluxes up to $\phi = 100$ kHz/cm^2. These requirements are driven by the identification of J/Ψ and Ψ' in the di-electron decay channel. Populations of J/Ψ and Ψ' (in particular the ratio of them) are considered as the most promising signatures of Quark Gluon Plasma and its evolution [8, 9]. However, the very small production yields (specially in the case of Ψ') demand very high interaction rates (up to 10^7 collisions per second), posing challenges for the detector technologies [5].

In this work the rate capability of classical MWPCs with a gap of $h = 3$ mm and $s = 3,4$ mm anode wire pitch has been explored, for binary gas mixtures Xe-CO_2, Ar-CO_2 and Ne-CO_2. CO_2 has been chosen as the UV-quencher due to its low chemical reactivity, non-flammability and very good ageing properties while we focused on Xe due to its high cross-section for X-ray absorption.

The data is interpreted within the theoretical framework developed by Mathieson and Smith ([10], [11]).

This document is structured as follows: the setup is described in section 2; once the characteristic gain vs voltage curve has been measured (section 3), the behavior of the gain as a function of the rate (section 4) can be described within the Mathieson model (subsection 4.1) after beam-size corrections are accounted for (subsection 4.2), allowing for a determination of the mobilities of the drifting ions (subsection 4.3). An extrapolation to the most common case of uniform illumination by minimum ionizing particles (mips), together with a discussion of the results is presented in subsection 4.4 and section 5, respectively.

2. Experimental setup and description of the measurements

The experimental setup is shown in Fig. 1. The chamber wires are made of gold-coated tungsten of 10 μm radius. The MWPC has a very thin entrance foil that acts as one of the cathode planes (25 μm aluminized kapton). The window dimensions are 6 cm $\times$ 8 cm but a slightly smaller fiducial area of 5 cm $\times$ 5 cm was determined as the region where the gain uniformity was below $\mathrm{rms}_m \leq 5\%$. The chamber was irradiated with an X-ray tube, collimated down to a nominal area of approximately $A \simeq 0.5$ cm^2, centered with respect to the afore-mentioned fiducial area. The estimation of A was done via simultaneous exposure of 10 Polaroid films attached to the window, producing images like the ones shown in Fig. 2 after developing the film. The duration of the exposure was chosen as much as possible such that the first films of the stack were over-exposed and the last under-exposed. By looking at the beam-profile as a function of the film number the beam-quality can be then assesed. The small presence of tails in some cases (Fig. 2, compare 2-up and 5-up) was taken into account as a 10% uncertainty in the area determined by this procedure.

Unless stated otherwise, all the measurements here presented have been performed with an X-ray tube operated at a voltage $V = 9$ kV, placed approximately 10 cm away from the chamber. By using different filters (0.25-0.5 mm thick Al foils) most of the low-energy bremsstrahlung and characteristic radiation can be suppressed. The feature-less bremsstrahlung spectra can, by means of this procedure, render a narrow structure close to the maximum photon energy.

The measured charge was calibrated by using as reference the internal conversion line of a Fe^{55} source ($E_{X-ray} = 5.9$ kV). Typical charge spectra measured with the ADC after calibration are shown in Fig. 3 for a Ar-CO_2(80-20) mixture, obtained with the source (squares) and with the tube (triangles, circles) for two different filters. The energy spectra obtained with a Fe^{55} source showed a peak-resolution $\sigma_E/\bar{E} = 10 - 20\%$ with a clear Argon escape peak placed at approximately one half of the total absorption one. The spectrum measured with the X-ray tube was broader ($\sigma_E/\bar{E} = 15 - 30\%$), resulting from the wider distribution of the bremsstrahlung photons.

In order to obtain the distribution of Fig. 3 the signal induced in both cathode planes was added and amplified by a custom-made charge sensitive pre-amplifier followed by an ORTEC 452 spectroscopic amplifier. The analog signal was duplicated with a linear Fan-in-Fan-out and sent to a LeCroy 0628 leading edge comparator and to a Lecroy 2249W charge ADC. The output of the former was used for gating the ADC and for the rate determination, via a scaler. The chamber current was measured with a Keithley 6487 amperemeter.

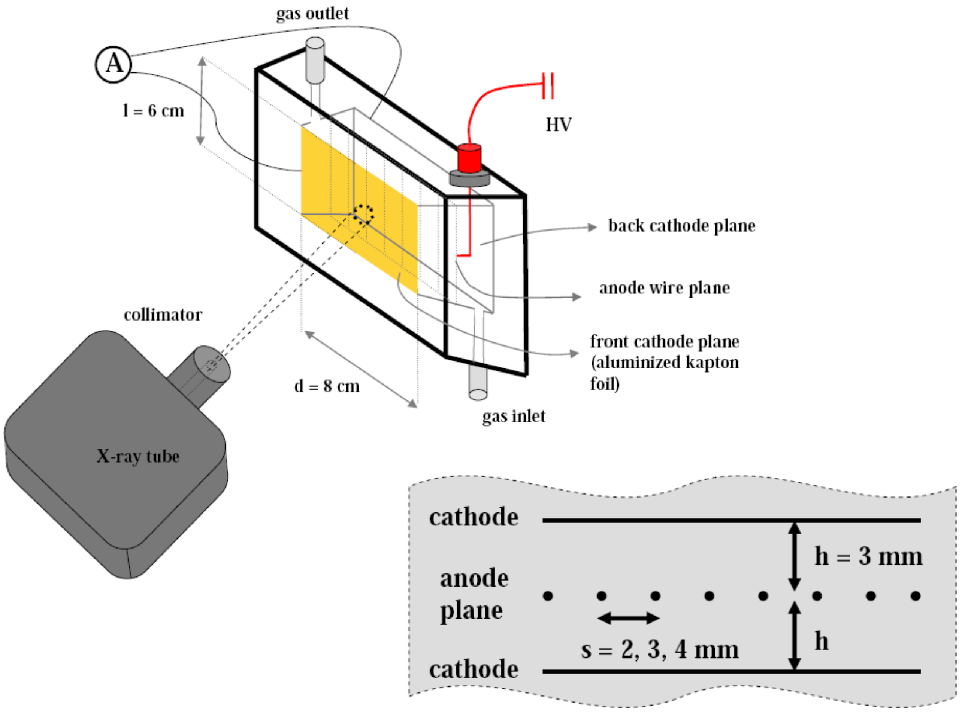


Figure 1. Experimental setup. The configuration sketched was chosen for current measurements, being the amperemeter denoted by -A-. For rate determinations the amperemeter was replaced by two amplifying stages and a linear Fan-in Fan-out with one output signal sent to the discriminator and scaler and the other one to the ADC.

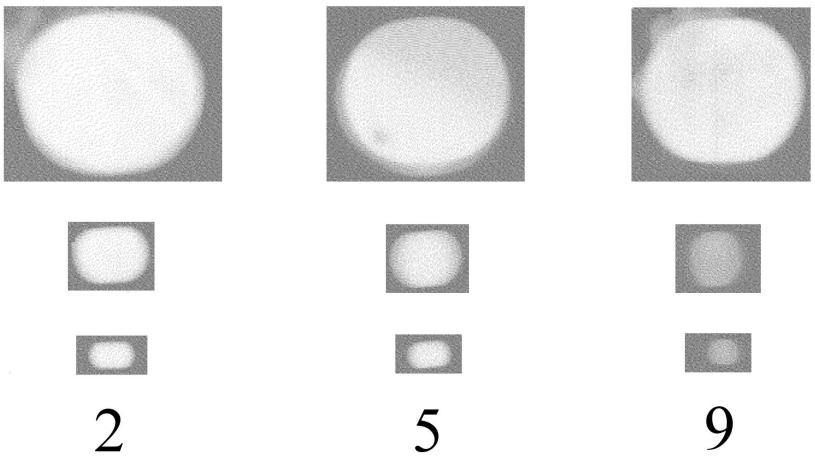


Figure 2. Illustration of typical beam spots in the Polaroid film stack as a function of the number of film. From top to bottom: $A = 143 \pm 14$ mm^2, $A = 36 \pm 3.6$ mm^2, $A = 6 \pm 0.6$ mm^2. Left-right shows the increasing direction (downstream) of film number. A typical choice for the determination of A is the central column (5). Film 2 is over-exposed. Comparison between 5 and 9 shows a spot fading away in a rather uniform manner, suggesting that the beam-spot in 5 is highly uniform, as expected.

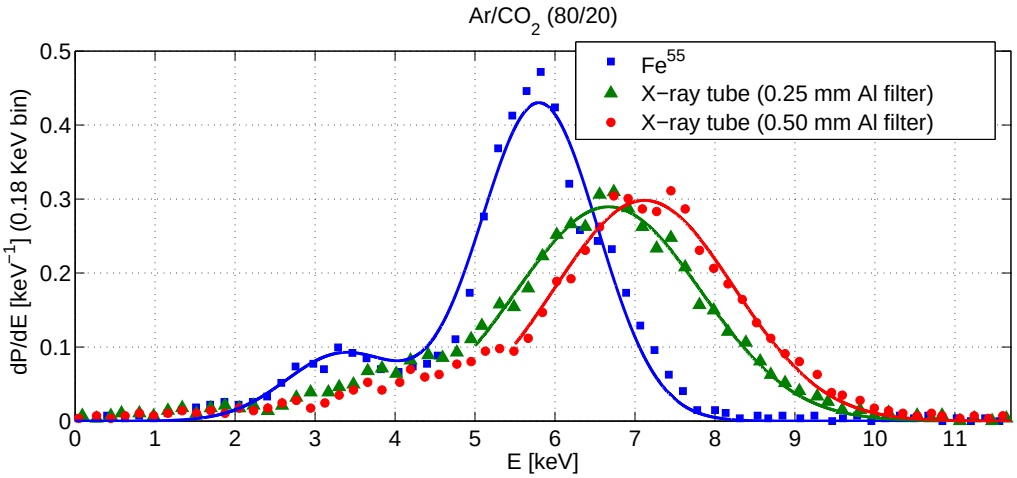


Figure 3. Energy loss spectra obtained with the s=4 mm anode-pitch MWPC after calibration. The characteristic escape peak from Argon is visible under illumination with a Fe^{55} source (resolution $\sigma_E/\bar{E} = 15\%$) but disappears when using the X-ray tube. The broader energy distribution in such a case stems from the non-monochromatic nature of the bremsstrahlung photons. Single (for the tube) and double (for the source) Gaussian distributions have been fitted to data.

Once the current and the avalanche rate are measured, the detector gain can be obtained as:

$$m = \frac{i}{n_o r} \tag{2.1}$$

where i is the total current, r the avalanche rate and n_o the average number of electrons initially released by the X-ray photon.

For studying the behaviour of the gain as a function of rate, the determination of the later can be simplified by resorting to its proportionality with the tube current, that was verified over the whole range. Only one direct determination of the rate (obtained at low rates) is therefore needed at the beginning of each 'rate scan' and higher values can be obtained by proportionality with the tube current.

In some particular cases like for the determination of the characteristic gain curves, where the nominal rate was not too high, it was useful to perform direct rate measurements with some regularity and care was taken of checking that the electronics dead-time had little impact in the results. The dead-time of the electronics system was estimated by resorting to the afore-mentioned proportionallity with the tube current: measurements were performed in pure CO_2 at $m \simeq 5 \times 10^4$ and a phenomenological model of only one parameter was used to fit the data (Fig. 4), yielding the correction formula needed translate the measured rate r_{meas} to the real rate r:

$$r = -\frac{1}{\Delta T} \ln(1 - \Delta T \; r_{meas}) \tag{2.2}$$

with ΔT in the range 2-3 μs, slightly depending on the gain and mixture. Due to this dependency, only dead-time corrections not in excess of 20% were allowed in practice.

A comparison between these two independent methods (proportionality with the tube current and dead-time correction) was nevertheless utilized as a cross-check in a number of cases, showing good agreement up to moderate rates. In general, the former method (proportionallity with the

tube current) was preferred for the measurements of the rate capability and the second (dead-time correction) for the determination of the characteristic gain curve. Faster electronics (required for the final application in CBM) is currently under development.

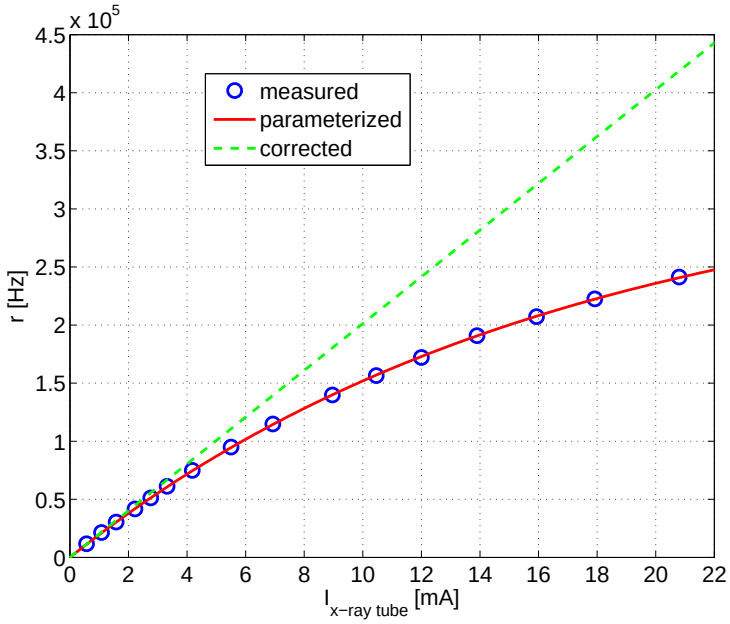


Figure 4. Electronic dead-time as measured in pure CO_2 at $m \simeq 5 \times 10^4$. The points indicate the measured rate as a function of the X-ray tube current. The continuous line is a 1-parameter phenomenological fit introduced in the text.

All measurements were performed in a monitored (not controlled) atmosphere with the temperature, pressure and oxygen content showing values in the range $T =$ 22-25 ^{o}C, $P =$ 985-1010 mbar, $f_{O_2} =$ 8-20 ppm. Fresh gas was injected at 2 detector volumes per minute. The voltage was corrected to the standard ambient value ($T_o = 20\ ^o$C and $P_o = 1000$ mbar) by introducing the reduced potential $V^* = \frac{P_o}{P}\frac{T}{T_o}V$, as is customary.

3. Gain curve measurements and chamber stability

The characteristic gain curve is a necessary input when attempting a quantitative description of the rate capability of MWPCs [10]. On the other hand, the maximum operating voltage before glow discharge or breakdown appears in a chamber must be also scrutinized critically. The measurements devoted to these aspects are compiled in this section.

The experimental determination of the gain curve is based on eq. 2.1. The chamber was irradiated with the X-ray tube and, after optimization of the filters and tube voltage, a spectrum with a peak energy of $\bar{E}_{X-ray} \simeq= 6.6$ keV and $15-30\%$ width (worsening when increasing the fraction of quencher) was produced. The main advantage of this procedure, as compared to irradiation with a Fe^{55} source, is that the very strong decrease in absorption cross-section with the CO_2 concentration (and therefore in counting rate) can be accommodated by adjusting the intensity of the tube with the additional help of 2 Al filters, so that the measurements of the characteristic gain curves can be

easily taken at the same avalanche rate. This approach largely increased the reproducibility of the measurements under different conditions.

Once the rate and the current are known, the gain can be calculated from eq. 2.1 and the initial number of electron-ion pairs n_o:

$$n_o = \frac{\bar{E}_{X-ray}}{W} \tag{3.1}$$

$$W = \left(\frac{1 - f_{CO_2}}{w_{noble}} + \frac{f_{CO_2}}{w_{CO_2}} \right)^{-1} \tag{3.2}$$

being W the effective average energy to produce one electron-ion pair, w_{noble} and w_{CO_2} the corresponding values for pure noble gas and CO_2, respectively, and f_{CO_2} the fraction of CO_2. A slight shift of the peak energy $\bar{E}_{X-ray} = 6.6 - 7.1$ keV was observed when using a second filter. This was taken into account for evaluation of eq. 3.1.

In order not to bring the amperemeter to the limits of its sensitivity, a primary rate $r = 120$ kHz was kept constant for the measurements at low gains ($m < 5 \times 10^4$), yielding a minimum current of 5 pA (corresponding to $m \simeq 1$) in pure CO_2. The chosen rate represents a compromise between a low system dead-time (Fig. 4) and small space-charge, on one hand, and a reasonable current at low voltages on the other hand. The uncertaintinty of the current was determined through the rms of 30 consecutive measurements, resulting in a statistical dispersion of $\simeq 1\%$. At $m \simeq 1$ the current stabilized only after several minutes (maximum 30 min), showing an uncertainty of $\simeq 10\%$.

Aiming at reducing the effect of space-charge in the characteristic curves, gains above $m \simeq 5 \times 10^4$ were determined at a reduced rate of $r = 10$ kHz. After correcting for the system dead-time both the high and low gain regimes were found to be in good agreement. No significant difference was observed between the gain curve obtained with the Fe^{55} source as compared with the tube, for a reference Ar-CO_2(80-20) mixture.

For illustration, the gain curves as a function of the reduced anode potential V^* are shown in Fig. 5 for the case of Xenon mixtures in the $s = 3$ and 4 mm -pitch chambers. The region $m = 1$ is well described when obtaining n_o from the tabulated values of Sauli [12], but an excellent agreement was also verified for the Ne and Ar mixtures. Overall, the behavior of both chambers is very similar, regarding voltage dependence. For chambers of pitch $s = 2$ mm (not shown) the gain curves are substantially different due to the increasing influence of the neighboring wires in the field close to the anode. A systematic study of the gain behavior of these chambers will follow to this publication.

Fig. 5 shows an exponential fit in the region $m = 10^3$ - 10^5 (solid line), that is used in the next section, together with an extrapolation to higher gains (dotted line). The deviation of data from the fit was identified as the onset of a self-sustained discharge in the chamber[1]. From the crossing point of the up-extrapolated gain (dotted line) and a linear down-extrapolation (dot-dashed line) of the last two data points one can obtain a crude estimate of the onset of the process. For Xe mixtures the chambers were stable up to a maximum gain $m_{max} = 3 \times 10^5$, being little dependent on the fraction of quencher. After prolonged operation in the discharge regime, the chamber required a power cycle to restore its previous performances.

[1]The chamber continues to draw the same current even when the tube is switched off. After little training, the process can be identified by direct observation in the scope.

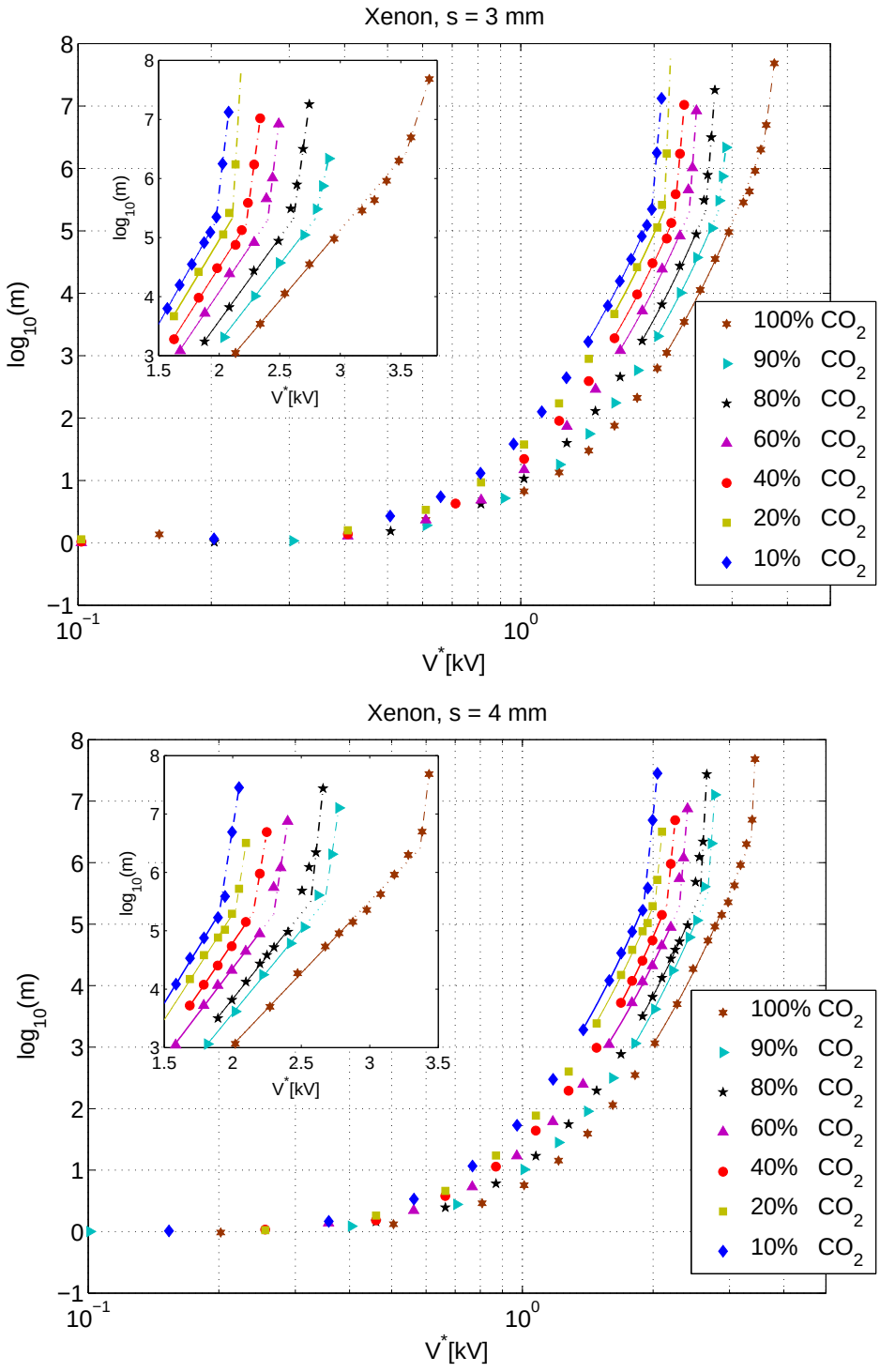


Figure 5. Up: gain m vs reduced voltage V^* for the $s = 3$ mm -pitch chamber operated in Xenon with different fractions of CO_2. Down: like up-picture but for the $s = 4$ mm -pitch chamber. The inset zooms in the region where data has been fit to an exponential ($\log_{10}(m) = 3-5$) and also the regime of self-sustained discharge ($\log_{10}(m) \gtrsim 5.5$).

4. Rate capability measurements

4.1 The Mathieson model

The theoretical description used in this work has been introduced elsewhere [10]. For simplicity, an exponential dependence of the gain with the applied voltage has been assumed, such that:

$$\ln(m) = aV + b \tag{4.1}$$

that is well satisfied for our chambers in the region $m = 10^3 - 10^5$, and is a convenient parameterization provided the gain was never reduced below those values, when operated at high photon fluxes. Following [10], the gain behaviour as a function of the flux can be expressed as:

$$m = m_o \exp\left(-q_e \frac{a^2(f)\, n_o(f)}{2\mu_\alpha(f)} \frac{sh^2\, \bar{d_m}(s,h)}{C_L(s,h,r_a)} \frac{m}{\ln m - b(f)} \phi\right) \tag{4.2}$$

with q_e being the electron charge, m_o the gain at zero rate, n_o the initial number of electron-ion pairs, μ_α the mobility of ion-specie α, f the fraction of quencher, C_L the wire capacitance per unit length and ϕ the avalanche flux (in $[T^{-1}L^{-2}]$). The correction for finite area of illumination, here denoted as $\bar{d_m}$, is a function defined between 0 and 1, that solely depends on the chamber geometry and the shape of the beam spot, under the assumptions of [10][2]. The functional expression of C_L is:

$$C_L = \frac{2\pi\varepsilon_o}{\ln(r_c/r_a)} \tag{4.3}$$

with r_a the anode radius and r_c being well approximated in the limit $s/h < 2\pi$ by:

$$r_c \simeq \frac{s}{2\pi} e^{\pi h/s} \tag{4.4}$$

It becomes apparent that, once the characteristic 'm vs V' curve has been measured (a, b are then known), the only free parameter for every mixture is $\mu_\alpha(f)$. Therefore, within the Mathieson model only one curve 'm vs ϕ' is needed experimentally for a given mixture (for any m_o) and the behavior for different m_o can be derived from eq. 4.2. Moreover, the mobility of the ions is usually well described by the Blanc's law [13], that in our case simply reads:

$$\frac{1}{\mu_\alpha} = \frac{1 - f_{CO_2}}{\mu_{\alpha,noble}} + \frac{f_{CO_2}}{\mu_{\alpha,CO_2}} \tag{4.5}$$

where $\mu_{\alpha,noble}$ and μ_{α,CO_2} are the mobilities of the drifting ion α in the corresponding pure gas. In case of pure gases the nature of α must change but, if two rate curves are obtained at, say, $f_{CO_2} = 20\%$ and $f_{CO_2} = 80\%$, then eq. 4.5 together with eq. 4.2 would allow for a complete characterization of the rate capability of the chamber for all the possible admixtures of two given gases (except maybe in the limit of pure gases). In general different drifting species may coexist, but on the basis of a generally accepted fast charge-transfer mechanism [12] only one drifting ion is considered here for each noble gas-CO_2 mixture, its nature not depending on the gas concentration (except maybe in the limit of pure gases). The complex nature of the ion drift and its high sensitivity

[2] In particular ion diffusion is not included in the model.

to the presence of impurities [13] advice, nevertheless, to verify Blanc's law experimentally for every particular case.

The main experimental difficulty involved in the precise evaluation of the rate capability of a chamber can be observed after inverting eq. 4.2: if the rate capability ϕ_F is defined as the flux needed for causing a certain fractional gain drop F, the following expression can be obtained:

$$\phi_F = q_e \frac{\ln((1-F)m_o) - b}{(1-F)m_o} \frac{2\mu_\alpha(f)}{a^2(f)\, n_o(f)} \frac{C_L(s,h,r_a)}{sh^2 \bar{d}_m(s,h)} \ln(1-F) \tag{4.6}$$

and making use of the fact that the logarithm is a slow varying function of its argument:

$$\frac{\delta\phi_F}{\phi_F} \simeq \frac{\delta F}{F} \tag{4.7}$$

Therefore, an experimental uncertainty in the determination of m_o by 5% will cause an uncertainty in the determination of the fractional drop at $F = 10\%$ by 50%, and this uncertainty will be directly propagated to the estimated rate capability.

An illustration of the measured gain behavior as a function of the avalanche flux is shown in Fig. 6 for the case of Xe-CO_2(90-10) and Xe-CO_2(80-10) in the $s = 4$ mm chamber. The statistical uncertainty is smaller than the size of the data points. Indeed, not all the mixtures were equally well characterized: in view of the final application of this work (TR detection) the measurements in Xenon were performed at 3-4 different values of m_o for every concentration of quencher f_{CO_2}. For Argon and Neon -based mixtures almost 2 curves at different m_o were measured in average for every value of f_{CO_2}. The flux ϕ has been already extrapolated to the case of uniform irradiation as $\phi \to \bar{d}_m\phi$, taking into account the finiteness of the beam-spot. As shown in the next section, the correction factor involved in such an extrapolation $\bar{d}_m$ amounts to $\simeq 0.5$ for the bulk of the measurements presented here.

4.2 Extrapolation to infinite area of illumination

The 'Mathieson model' includes a prescription on how to correct for finite beam size effects ([10], [11]) and even extraordinary experimental agreement has been found for the 1-D case [14] (finite irradiation along the direction of the wires, infinite in the transverse direction). To the authors' knowledge, no dedicated study exists for the 2-D case.

Following the original formulation of Mathieson, the voltage drop $\Delta V(x,y)$ at the anode plane caused by a charge distribution with a certain x-y profile can be obtained from an electrostatic calculation assuming a constant space-charge density of the drifting ions in the chamber. A correction factor can be then introduced as:

$$d_m(x,y) = \frac{\Delta V(x,y)}{\Delta V_o} \tag{4.8}$$

where ΔV_o is the voltage drop at the anode plane in case of uniform/infinite irradiation. A calculation of the factor $d_m(x,y)$ for a squared beam profile[3] can be accomplished by using expressions in [15], yielding:

$$d_m(x,y) = \frac{8}{\pi^2 h^2} \int_o^\infty \int_o^\infty dk_1 dk_2 \frac{\sin(k_1 H/2)\sin(k_2 L/2)\cos(k_1 y)\cos(k_2 x)}{k_1 k_2 (k_1^2 + k_2^2)}$$

[3]The experimental oval-like beam-spot will be assimilated to a square, for the sake of simpler theoretical description.

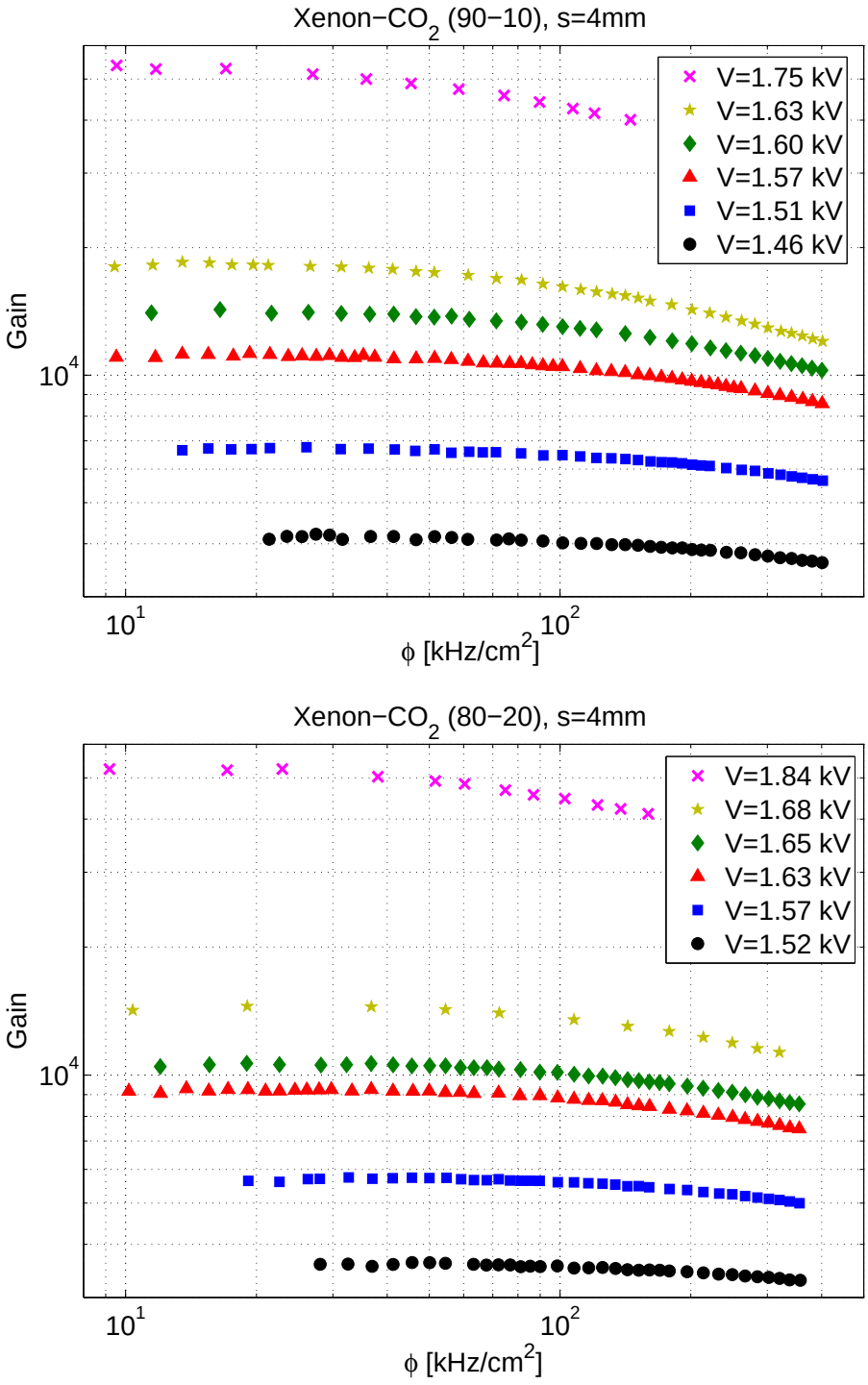


Figure 6. Up: gain as a function of the avalanche flux for the $s = 4$ mm chamber operated in Xenon with 10% CO_2. Down: like up-figure but for 20% CO_2. The flux has been extrapolated to the case of uniform irradiation. This correction implies a scaling-down of the measured flux by a factor 2 for our setup (see text).

$$\times \left[1 - \frac{1}{\cosh\left(h(k_1^2 + k_2^2)^{1/2}\right)} \right] \tag{4.9}$$

Following the notation of [11], L is the beam size along the wires (x axis) and H across them (y axis). When $H \to \infty$ (1-D limit) $d_m(x,y)$ must be averaged in the interval $\pm L/2$ in order to obtain the desired correction factor, as has been shown in [10]. This factor as in eq. 4.2 would be naturally interpreted as an 'effectively' reduced flux $\bar{d_m} \times \phi$ or, equivalently, as a certain particle rate over an 'effectively' increased area, as compared to uniform irradiation. Remarkably, according to [10] the correction factor $\bar{d_m}(L,H,s,h)$ depends only on the chamber/beam arrangement.

Despite this apparent simplicity, the 'effective' voltage distribution at the wire positions y_k ($\Delta V_e(x,y_k)$) seems to be needed in order to generate the exact 2-D distribution $\Delta V(x,y)$ that allows for a precise description of data [14]. A generalization to the 2-D case by averaging $d_m(x,y)$ over the H/s irradiated wires was introduced in [11] based on the magnitude $\Delta V_e(x,y)$. The original approximation will be used in this work, $\Delta V(x,y_k) \simeq \Delta V_e(x,y_k)$, for the sake of simplicity, so that eq. 4.9 can be used directly.

In the continuous case where the density of wires is infinite, a direct integration of eq. 4.9 yields the desired average:

$$\bar{d}_{m,c} = \frac{1}{LH} \int_{-L/2}^{L/2} \int_{-H/2}^{H/2} d_m(x,y)\,dy\,dx \tag{4.10}$$

while in the discrete case the integral over y must be replaced by a discrete average at the position of the wires:

$$\bar{d_m} = \frac{1}{NL} \int_{-L/2}^{L/2} \sum_{k=1}^{N} d_m(x,y_k)\,dx \tag{4.11}$$

where k runs up to the N wires within the area of illumination. If the discretization of space would influence the value of $\bar{d_m}$ also the relative position chamber-beam will. This was evaluated by simulating chamber-beam displacements along y in 0.25mm intervals for different pitches $s = 3,4$ mm and a beam-spot $L \simeq H \simeq 6$ mm, yielding a deviation from the continuous value $\bar{d}_{m,c}$ within $\pm 10\%$.

In order to better assess the role of the beam size, a specific set of measurements of the rate capability at various beam sizes was accomplished. Taking advantage of the fact that the correction factor $\bar{d_m}(h,s,L,H)$ should not depend, within the model, on the gas mixture, its value was evaluated from measurements of the rate capability at 10% drop (ϕ_{10}) in pure CO_2 (Fig. 7). The correction factor was obtained experimentally after normalizing by the rate capability obtained at infinite beam size $\bar{d_m} = \phi_{10}(\infty)/\phi_{10}(L)$. The value of $\phi_{10}(\infty)$ was determined as the average of the three rate capabilities measured at the largest beam profiles.

Fig. 7 shows the behavior of $\bar{d_m}$ both in data (triangles) and model (circles) for a square profile, together with a phenomenological 2-parameter fit to a function $\bar{d_m} = 1 - \exp(-L/{L_o}^c)$ (continuous line). The theoretical value of $\bar{d_m}(L)$ tends asymptotically to 1 although slower than one may expect (even for $L = 20$ mm ($\gg s,h$) the required correction factor is still at the level of 20%)[4] and, conversely, it drops to zero very fast when $L \simeq s,h$, as also seen in data. Since data, model and fit

[4]To reduce the correction below 5% would require of a square spot with its side being larger than 10 cm.

agree reasonably well for our nominal beam profile $L \simeq 6$mm, a value of $\bar{d_m} = 0.5$ was taken for extrapolating the measured fluxes to the uniform irradiation case, and a 20% overall uncertainty was estimated for the flux calculated following this procedure. This value corresponds approximately to the uncertainty of the mean of the three highest points in Fig. 7 that was experimentally defined as $\phi_{10}(\infty)$.

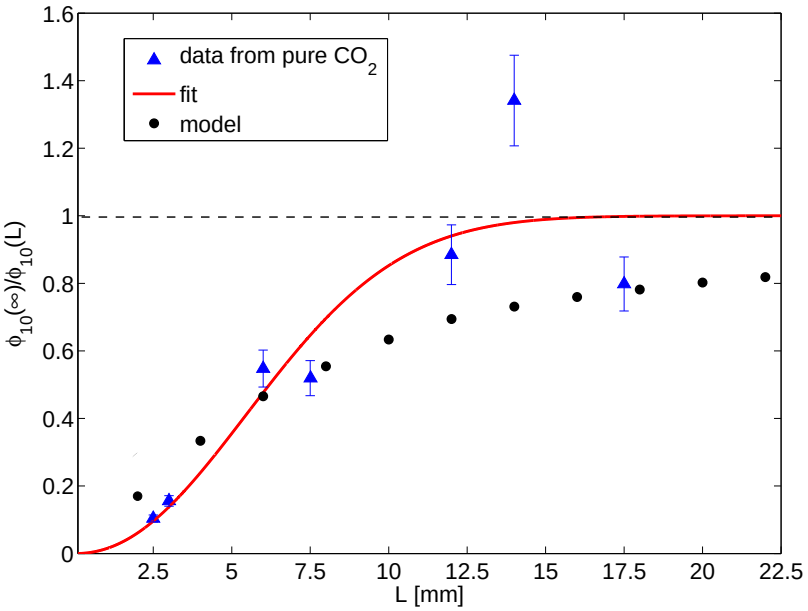


Figure 7. Comparison between data (triangles) and model (circles) for the correction factor $\bar{d_m} = \phi_{10}(\infty)/\phi_{10}(L)$. $\bar{d_m}$ has been experimentally defined as the ratio of the flux at 10% gain drop for infinite area of irradiation divided by the one measured for a square beam of side L. $\phi_{10}(\infty)$ is defined as the average of the three higher points. Data has been taken in pure CO_2. A 2-parameter fit is shown also as a continuous red line.

4.3 Fitting procedure

A simultaneous description of all data based on eqs. 4.2 and 4.6 (Mathieson model including Blanc's law) is presented in this section. Following the spirit of [13] no assumption is done regarding the nature of the drifting ion that is denoted by α (in Xe), β (in Ar) and δ (in Ne). There are therefore 6 free parameters, namely: μ_{α,CO_2}, $\mu_{\alpha,Xe}$, μ_{β,CO_2}, $\mu_{\beta,Ar}$, μ_{δ,CO_2}, $\mu_{\delta,Ne}$. A global fit of the gain vs flux curves for the 3 mm -pitch chamber (36 data sets) and the 4 mm -pitch chamber (52 data sets) was therefore attempted by using the 6×2 free parameters introduced above (2 for each noble gas-mixture). The transcendental equation 4.2 was evaluated numerically by interpolation after being tabulated first.

A χ^2 minimization was performed by assigning equal weight to the data sets for every mixture. This means that each residual is normalized by the measured value and each data set is additionally weighted by the number of data sets availables per mixture (for instance, the residuals for each data set for the Xe-CO_2(90-10) mixture in s=4 mm (6 in total) are correspondingly divided by 6, Fig.

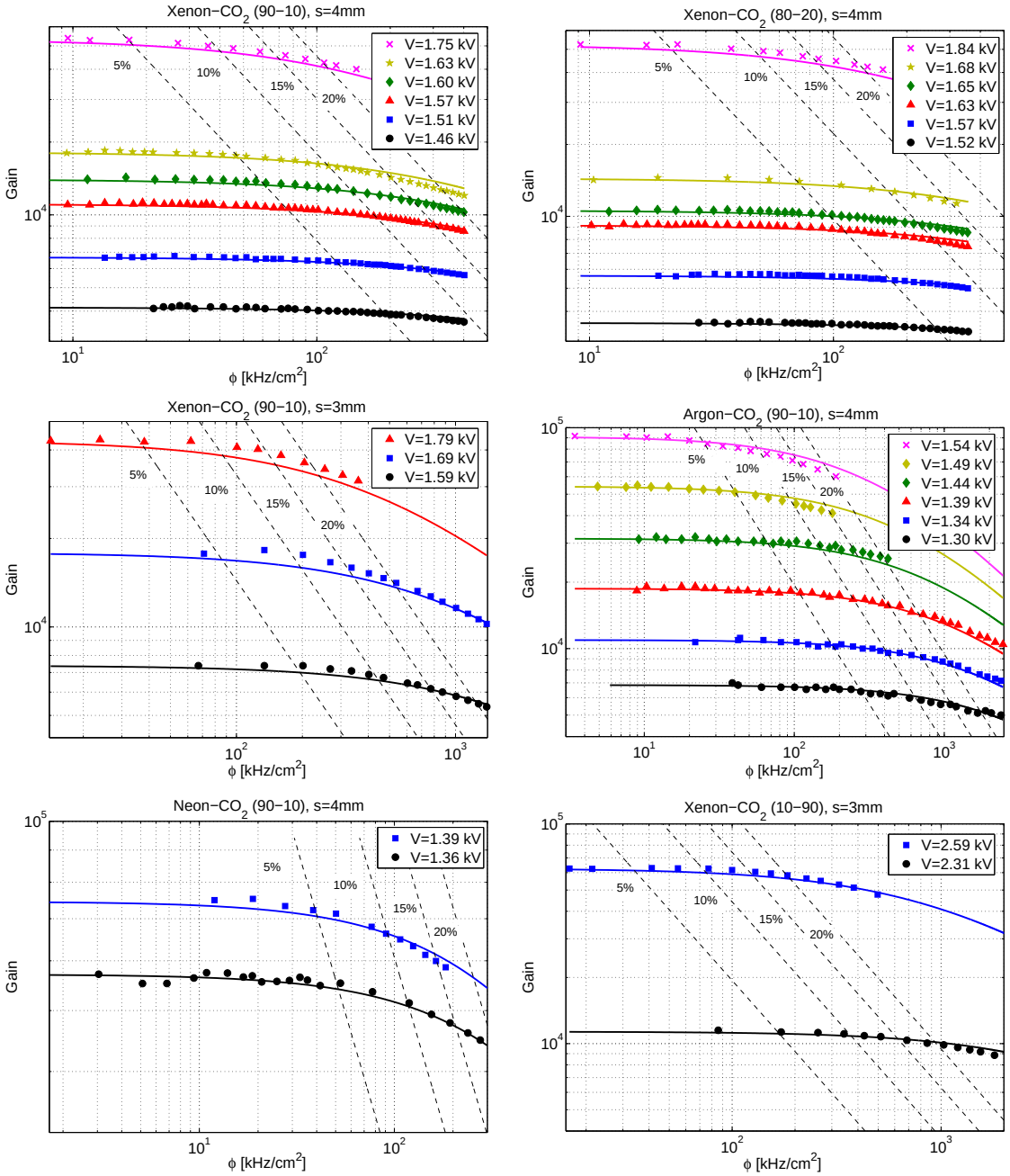


Figure 8. Up-left: fit of the rate curves for Xe-CO_2 $(90-10)$ obtained for the $s = 4$ mm chamber. Up-right: the same as up-left but for $80-20$ admixture. Center-left: the same as up-left but for $s = 3$ mm. Center-right: the same as up-left but for Ar-CO_2. Down-left: the same as up-left but for Ne-CO_2. Down-right: fit of the rate curves for Xe-CO_2 $(10-90)$ obtained for the $s = 3$ mm chamber. Dashed lines represent the theoretical flux at given fractional gain drops from the Mathieson formula with parameters obtained from the fit. A total of 88 curves/data sets have been fitted simultaneously.

6-up). This procedure avoids that the fit is dominated by high gains, and compensates for the fact that not all gas mixtures are equally well represented in terms of data sets (see app. A).

Two main sources of uncertainties were identified:

1. One is related to the estimate of m_o that is obtained for each data set as the average of the 3 gains measured at the lowest rates. This procedure works generally very well but in some cases there were not enough points for a good determination. Estimates of m_o wrong by few percent are very critical (eq. 4.7) and, indeed, a typical disperssion of 1% is present in data. In order to calculate the error introduced in the fit due to this effect, m_o was globally scaled up and down for all data sets in the range $\pm 3\%$ in steps of 1% and the fit performed afterwards. The parameters' uncertainties were estimated from the rms of the values obtained from these different fits.

2. A second source of uncertainty comes from the fact that the measurements were taken along 3 major campaigns and 3 (slightly) different beam sizes were used. Extrapolations to uniform irradiation were made according to Fig. 7 for which a systematic error of 20% in the re-calculated flux was assigned.

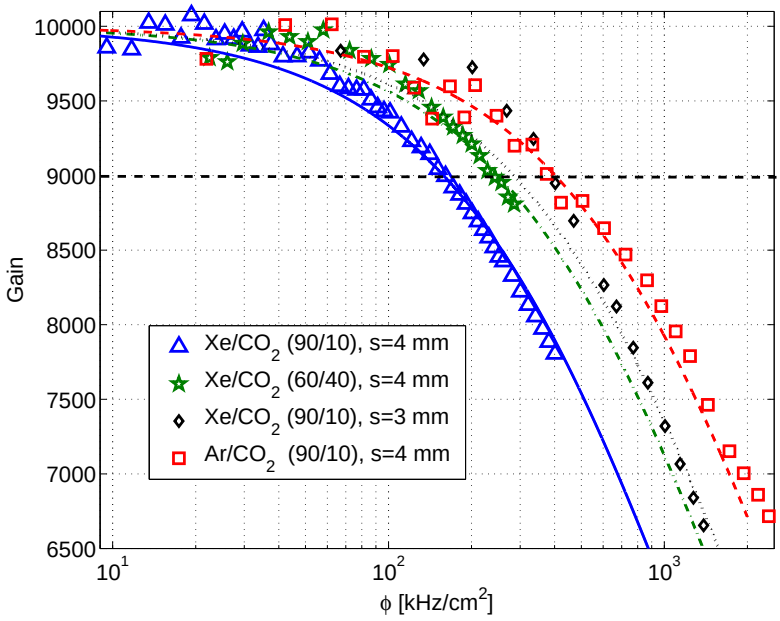


Figure 9. Compilation of different curves extrapolated to a typical gain $m_o = 10^4$. Figure aims at illustrating the main dependences of the rate capability, together with a detailed comparison with the theoretical model (lines).

The fitted data are compiled in the appendix A while some relevant cases are presented in Fig. 8, in order to illustrate the basic dependencies of the rate capability. The curves at fixed fractional drop are shown ($F = 5\%, 10\%, 15\%, 20\%$), obtained from evaluation of eq. 4.6 after substitution of the parameters of the fit.

A different attempt to extract dependencies can be performed by comparing at fixed gain. This is largely facilitated if the predicted scaling with m_o from eq. 4.6 is used:

$$\frac{\phi_F(m_o)}{\phi_F(m'_o)} = \frac{\ln((1-F)m_o) - b}{\ln((1-F)m'_o) - b} \frac{m'_o}{m_o} \tag{4.12}$$

The second term corrects linearly for the different total charge while the first incorporates the linear dependence of the drift velocity with the anode potential. Different dependencies can be therefore made more apparent, as shown in Fig. 9. The data sets have been chosen so that a (relatively small) extrapolation by using eq. 4.12 is done for a ratio $(m_o - m'_o)/m_o$ smaller than 50%.

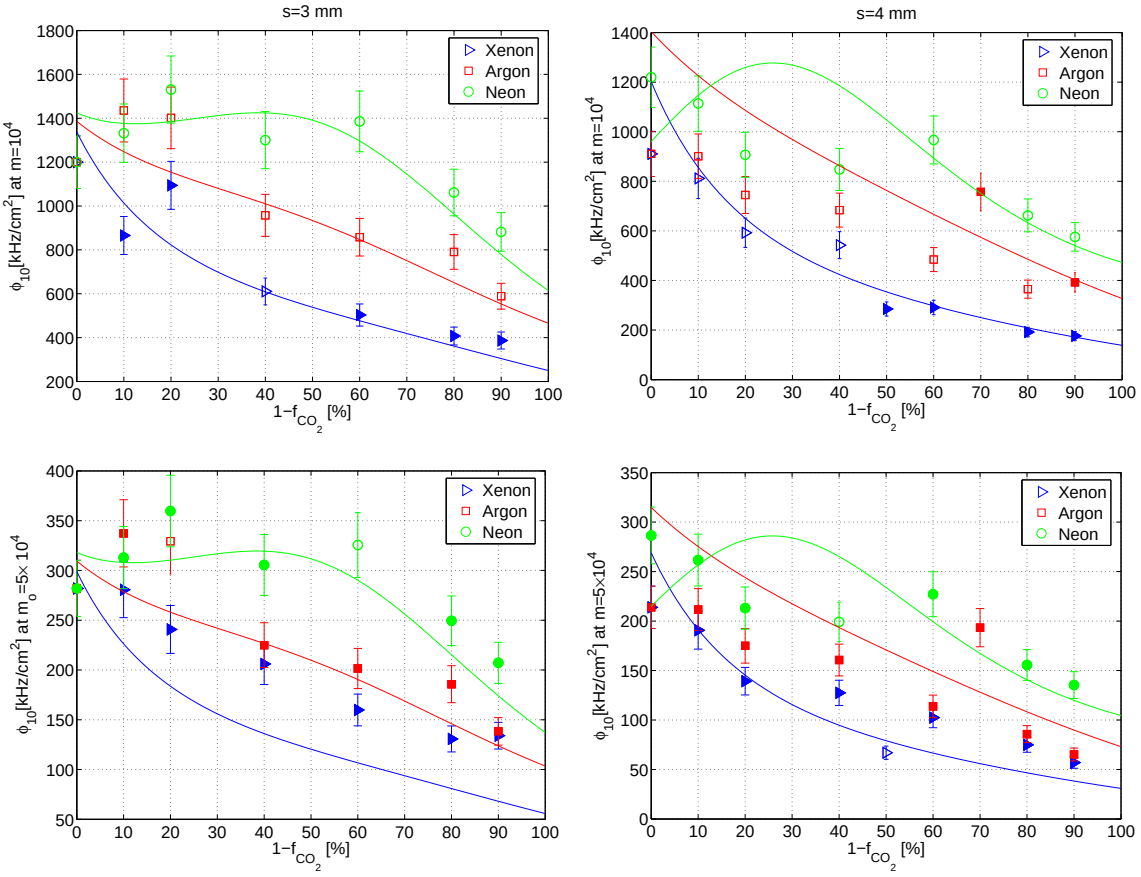


Figure 10. Up-row: rate capability at 10% gain drop for the $s = 3$mm and $s = 4$mm pitch chamber at $m_o = 10^4$ as a function of the fraction of noble gas. Data correspond to Xenon (triangles), Argon (squares) and Neon (circles) based mixtures. Open symbols indicate that the plotted value has been extrapolated over more than 50% difference with respect to m_o. Lines show the Mathieson model with the mobilities for the drifting ions taken from a global fit to 88 data sets. Low-row: as up-row but for $m_o = 5 \times 10^4$.

A more systematic approach can be still devised: the flux for a 10% fractional gain drop from a nominal gain m_o ('ϕ_{10} at m_o') can be experimentally determined by extrapolation from the closest value measured at m'_o, according to eq. 4.12. The main uncertainty in the determination of ϕ_{10} is the uncertainty in the measurement of m_o, that has been assumed to be 1%. By resorting to eq. 4.7, an uncertainty of 10% in ϕ_{10} has been estimated.

The resulting ϕ_{10} points can be plotted as a function of the fraction of noble gas, as shown in Fig. 10 for Xenon (triangles), Argon (squares) and Neon (circles) mixtures, for different pitches (s) and initial gains (m_o). Full points indicate that the extrapolation has been done from a curve measured with a real gain m'_o within less than 50% deviation from the extrapolated m_o. The lines represent the fit to the 'Mathieson model with Blanc's formula'. For convenience, the dependence

of the gain parameters a and b with f_{CO_2} has been parameterized by using 3^{rd} order polynomials.

The fitted mobilities used as input for the model are compiled in table 1, with their statistical and systematic uncertainties. The later (20%) arise from the uncertainty in the flux determination due to the beam size correction, that is reflected linearly in the measured mobilities (eq. 4.6). This uncertainty is a correlated one for all the measurements. The following features can be observed: i) the values of fitted mobilities in the $s = 3$ and 4 mm chambers are compatible within 1σ with exception of $\mu_{\alpha,Xe}$ and μ_{β,CO_2} (2σ), ii) the mobilities in noble gases differ in a ratio $\simeq 1:3:4$ for Xe:Ar:Ne. iii) When the results from the two chambers are combined, ion mobilities in Xe, Ar and Ne differ with a statistical significance of more than 2σ while all the mobilities in pure CO_2 are statistically compatible within 1σ, iv) the values of $\mu_{\alpha,Xe}$ are slightly higher than expected for Xe^+ but slightly smaller than other indirect measurements as [14], v) the mobilities of ion β in Ar and CO_2 agree well within errors with the CO_2^+ hypothesis, as has been measured for similar chambers [13], vi) ion δ shows a mobility much closer to the value of Ne^+ than CO_2^+ (factor two difference), vii) the average χ^2 is 0.99, providing statistical support to the approach followed in this analysis. A compilation of these mobilities can be found in [16].

mobility [$mm^2V^{-1}s^{-1}$]	$s = 3$ mm (fit)	$s = 4$ mm (fit)	mean	χ^2
μ_{α,CO_2}	$155 \pm 37 \pm 31$	$124 \pm 16 \pm 25$	$129 \pm 15 \pm 26$	0.59
$\mu_{\alpha,Xe}$	$70 \pm 6 \pm 14$	$95 \pm 13 \pm 19$	$74 \pm 5 \pm 15$	3
μ_{β,CO_2}	$173 \pm 18 \pm 35$	$128 \pm 24 \pm 25$	$157 \pm 14 \pm 31$	2.25
$\mu_{\beta,Ar}$	$214 \pm 20 \pm 43$	$207 \pm 30 \pm 41$	$212 \pm 17 \pm 42$	0.0377
μ_{δ,CO_2}	$126 \pm 23 \pm 25$	$129 \pm 25 \pm 26$	$127 \pm 17 \pm 25$	0.0081
$\mu_{\delta,Ne}$	$298 \pm 21 \pm 60$	$289 \pm 30 \pm 58$	$295 \pm 17 \pm 59$	0.0604

Table 1. Ion mobilities from the global fit of the data to the Mathieson model. The first errors are statistical, the second ones systematic.

4.4 Calculations for minimum ionizing particles

In the CBM experiment at FAIR, most of the particles over the anticipated MWPC-based TRD will be minimum-ionizing particles (mips) [5]. It is therefore important to estimate the rate capability in such an environment. A systematic survey of energy loss in Xe-CO_2 has been recently carried out over a broad dynamic range [18] where a detailed comparison between data and simulation was presented. A calculation purely based on the Bethe-Bloch formula overestimates the measured energy loss by some 30%. Hence, for simplicity, the Bethe-Bloch prescription as recommended for mixtures [19] was used here, but with a normalization taken to reproduce the value $dE/dx = 5$ keV/cm for $p = 1$ GeV pions in Xe-CO_2(85-15) reported in [18]. When going from pure Xenon to pure CO_2 such a procedure predicts a reduction in energy loss by a factor of 2, due to the smaller density. On the other hand, in the above-mentioned reference gas mixture the energy lost by mips is approximately 3 keV in the total gas thickness $2h = 6$ mm, to be compared with our X-ray energy $\bar{E}_{X-ray} = 6.6$ keV.

The compilation of the measured rate capability in Xenon mixtures for the $s = 3$ and 4 mm pitch chamber, extrapolated to mips by using the Bethe-Bloch formula obtained as explained above,

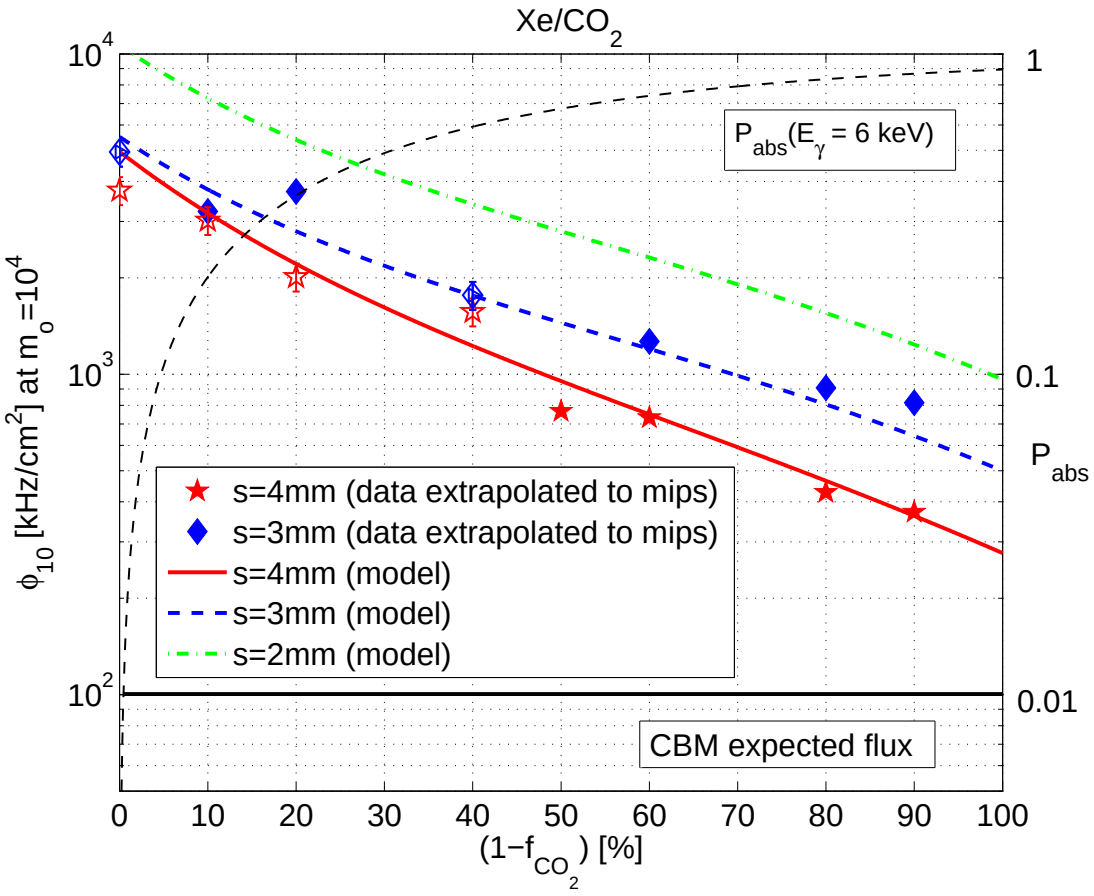


Figure 11. Up: rate capability at 10% gain drop for the $s = 3$ mm (diamonds) and $s = 4$ mm (stars) chambers extrapolated to minimum ionizing particles. The lines show the Mathieson model without fit. The extrapolation to the $s = 2$ mm case is also indicated (dot-dashed line), by using the mobilities of the $s = 3$ mm chamber from table in text (the necessary parameters of the characteristic gain curve are taken from measurements). The dotted curves (scale on the right) correspond to the absorption probability (P_{abs}) of X-rays of $E = 6$ keV. Open points indicate that the data has been extrapolated to m_o from a measured value m'_o different by more than 50%.

together with the model and an extrapolation to $s = 2$ mm is shown in Fig. 11 for a typical operating gain of $m_o = 10^4$ (extrapolation to $s = 2$ mm indeed requires to use the gain curves measured in such a case, that will be published elsewhere).

The improvement of the rate capability with decreasing s has two main origins: first, the rate per wire is proportionally smaller in such a case; second, the higher wire density implies that higher fields are required in order to get similar gains, meaning that the coefficient a becomes smaller (eq. 4.1). The fact that the gain curve is 'softer' in the sense of a being smaller makes the chamber more resistant to the space-charge of the ions ($\phi_F \simeq 1/a^2$). The capacitance per unit length C_L has little impact for normal values of s.

On the other hand, the behavior of the rate capability with increasing fraction of CO_2 has four main dependencies: i) The energy required to create a pair in CO_2 is higher than in noble gases (exception is Neon, where both are comparable). Still, this fact can account for a 30% increase

in Xe-CO_2 mixtures due to the lower initial number of electron-ion pairs when increasing the concentration of CO_2. ii) CO_2 is less dense than the mixture by a factor amounting by maximum 2 in Xenon-based mixtures, increasing the rate capability accordingly when going from pure Xe to pure CO_2. iii) The curves become 'softer' when the fraction of CO_2 is increased, resulting in an increase by a factor 2-3 from pure Xe to pure CO_2. iv) The mobility of the ions can vary also sizably between extreme cases: in case of Ne this implies a reduction of up to a factor 3 when increasing f_{CO_2} while in Xe it increases by a modest 50% when going from pure Xe to pure CO_2. These effects compete in some cases, as in Neon, where the increase in rate capability due to the much increased mobilities at high Neon concentration is compensated by a much harder gain curve. This yields a largely flat dependence of the rate capability for X-ray photons as a function of CO_2 concentration (Fig.10). In Xe mixtures all effects i-iv go in the same direction, and up to one order of magnitude can be gained in rate capability for minimum ionizing particles, between pure CO_2 and pure Xe, as shown in Fig. 11-up.

The present model has been used to describe recent mips data from M. Petris et al. [17], showing a good agreement. Nevertheless, we believe that the very small deterioration of the performances observed by the authors does not add extra support to the message conveyed in the present work.

5. Discussion

Considerable attention has been devoted in this work to the 'beam-size' correction. Nevertheless, if the model assumption that 'the correction factor $\bar{d_m}$ depends only on the chamber/beam arrangement' would hold true one could eventually resort, in general, to the well measured CO_2^+ mobility in CO_2 to estimate the factor $\bar{d_m}$ by imposing agreement with the Mathieson formula 4.2 in the limit of pure CO_2 (see [20]). Instead, if one would resort to the theoretical model to calculate it, a correction factor that would include i) an accurate knowledge of the beam intensity profile and ii) the relative beam/chamber alignment would be needed in order to obtain a precise (yet model-dependent) correction. Using the known CO_2^+ mobility in CO_2 as a reference or, alternatively, taking one single measurement with defocused beam should be probably more sound than attempting a detailed calculation. Overall, we consider the results of table 1 as a strong indication that reliable predictions can be done for the rate capability of MWPCs once the proper geometric corrections are performed and the nature of the drifting ion is known (and its mobility has been measured before). Within the precision of the present approach, Blanc's law works well. There is, nevertheless, a tendency of the Argon and Xenon mixtures to behave similarly at high gains ($m_o = 5 \times 10^4$), a fact that cannot be accomodated in the model.

With all the above information at hand, we are in position for discussing the more convenient MWPC geometry for the envisaged application in CBM. Due to the nature of TR, hadron identification/suppression worsens at low momenta where the particle deviates from the minimum ionizing regime. Additionally, the nature of the CBM spectrometer makes the detection of high energy electrons specially relevant in the context of J/Ψ and Ψ' detection, while the low momenta regime is well covered by the anticipated RICH detector and the TOF wall. Based on that we take as a working number the average TR energy released by a $p = 2$ GeV electron in a typical CBM-radiator, that is approximately $\bar{E}_{TR} \simeq 6$ keV [5]. This roughly corresponds to the minimum

momentum for which the CBM TR system will provide sufficient e/π suppression, and that we consider as our benchmark here. From the tabulated X-ray absorption in Xenon a mean free path of $\lambda_\gamma(E = 6\text{keV}) = 2.7$ mm can be readily obtained, being the probability to absorb the photon in the gas given by $P_{abs} = 1 - \exp(-2h/\lambda)$. High absorption probability must be balanced with a moderate rate capability, that has a steep dependence with the gap size (eq. 4.6).

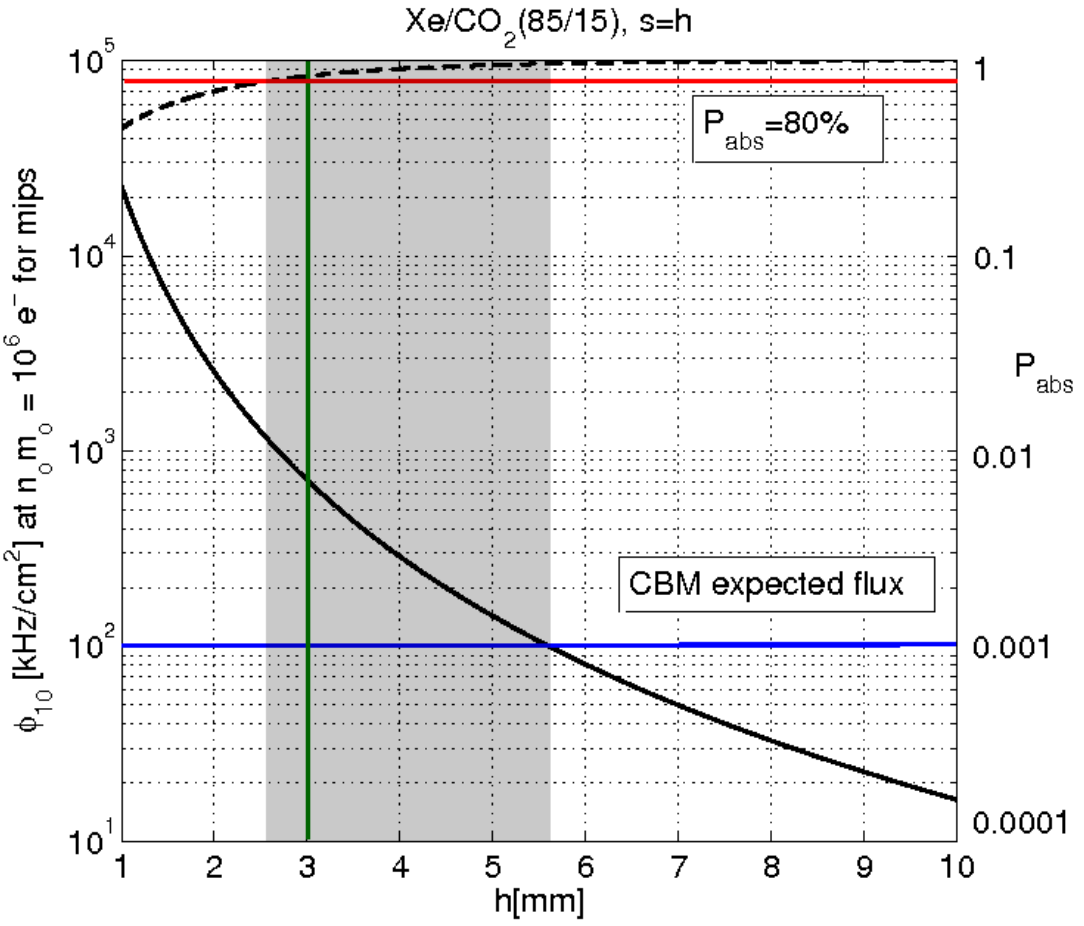


Figure 12. Extrapolated rate capability of a MWPC operated in a Xe-CO_2(85-15) mixture as a function of the chamber gap h for mips (axis on left) when the average signal amplitude in number of electrons is fixed to 10^6 e^- and $s = h$. The absorption probability of TR photons for the CBM benchmark case is shown with axis on the right (dashed line). The shadowed area represents a comfortable situation in terms of rate capability and photo-absorption probability. Mobilities have been taken from the weighted average of the mobilities in the $s = 3$ mm and $s = 4$ mm chambers, as obtained from the global fit to the Mathieson model.

A meaningful determination of the rate capability as a function of h can be accomplished by making some further assumptions: first, in order to avoid potentially harming operating voltages, the ratio s/h is kept constant. Second, the operating conditions are assumed to be such that the average number of electrons after multiplication is constant and equal to $n_e \simeq 10^6 e^-$ for mips (changes in h lead to changes in the initial ionization, that must/can be compensated by re-adjusting the gain, so that the induced signal is roughly the same). It is also possible to directly obtain the

rate capability dependence from a direct evaluation of eq. 4.6, when recalling the proportionallity of n_o with h, but at the price of a reduced signal for small h. In either one case or the other the implicit assumption that the gain curve is not strongly depending on h must be made, and only then an actual $1/h^3$ behavior (slightly modified by C_L) can be obtained for the rate capability.

Fig. 12 shows the expected behavior of the rate capability for MWPCs operated in Xe-CO_2(85-15) as a function of the anode-cathode gap h under the former assumptions, together with the absorption probability for our benchmark case in CBM ($\bar{E}_{TR} \simeq 6$ keV). Indeed, a very narrow set of values can be considered as satisfactory ($h = [2.5 - 5.5$ mm$]$), with the minimum value determined by the condition $P_{abs} > 80\%$ and the maximum by $\phi_{10} > 100$ kHz/cm.

Being the gap dependence so critical for MWPCs in terms of photo-absorption probability, it is worth discussing the possibility of using a drift region (of length D). For typical pad sizes of 1 cm^2 [7], the maximum CBM fluxes would imply a particle load of $1/10$ μs per channel causing a 10% pile-up probability within 1 μs. Taking the measured drift times in [4], even in a small drift region corresponding to $D = 2h$, the electron drift would extend up to a typical time of that order [4], making accurate charge measurements very difficult.

On the basis of the above arguments, staying at a MWPC configuration seems to be the most convenient solution for the CBM TR-detector. The possibility of using a mirrored configuration [7] with 3 cathode planes deserve further consideration, since it increases the X-ray detection probability while keeping the rate capability. If this improvement is worth the extra mechanical complexity or not, will be clarified when the first real size prototypes are built.

6. Conclusions

We conducted systematic measurements of thin MWPCs ($h = 3$ mm, $s = 3,4$ mm) filled with Xenon-CO_2, Argon-CO_2 and Neon-CO_2 mixtures under different fractions of quencher and at different gains. Employing the Mathieson model (including finite beam corrections) and the additive Blanc's law for ion mobilities the measured rate capability can be well described theoretically.

When aiming at efficient TR detection at high rates there is a narrow parameter-space where MWPCs are advantageous. The reason for that is the steep dependence of the rate capability with the chamber gap h as $\simeq 1/h^3$ opposed to the exponential behavior of the X-ray absorption probability $P_{abs} = 1 - \exp(-2h/\lambda)$. We found a good compromise in the value $h = 3$ mm where we can comfortably hold rates above 100 kHz/cm^2 as demanded by the TRD of the CBM experiment, while keeping a typical X-ray absorption probability above 80%.

Acknowledgments

DGD was supported by EU/FP6 contract 515876. The authors want to thank Christian Schmidt for discussions and kind help. Special thanks to M. Ciobanu for his valuable support with analog electronics and to J. M. Saa for his help with the bibliography on noble gases properties. We benefited from the collaboration of A. Battiato, G. Hamar, E. L. Gkougkousis and S. Kohl.

A. Results of the fit

A compilation of data for 36 mixtures (from a total of 44), fitted according to the procedure introduced in section 4.3, is presented here. The 8 missing plots are not shown (but included in the fit) for easier graphical representation. Data for each pitch and noble gas mixture (for all measured concentrations of the two gases) have been fit with 2 free parameters, namely the mobilities of the drifting ion in the pure gases. Due to the main scope of this work, data from Xenon at different 'low rate' gains m_o are more abundant than from Argon and, specially, Neon. For the later, only 1-2 curves are taken per mixture, a choice that relies on the trivial scaling of m_o predicted by the Mathieson model (eq. 4.12). Each mixture enters in the fit with the same weight, meaning that the residuals for each curve are divided by the number of curves per mixture (for instance, the residuals in Xe-CO_2(90-10) are divided by 6). The residuals are additionally divided by the measured value, in order that all data sets enter with the same weight for a particular mixture.

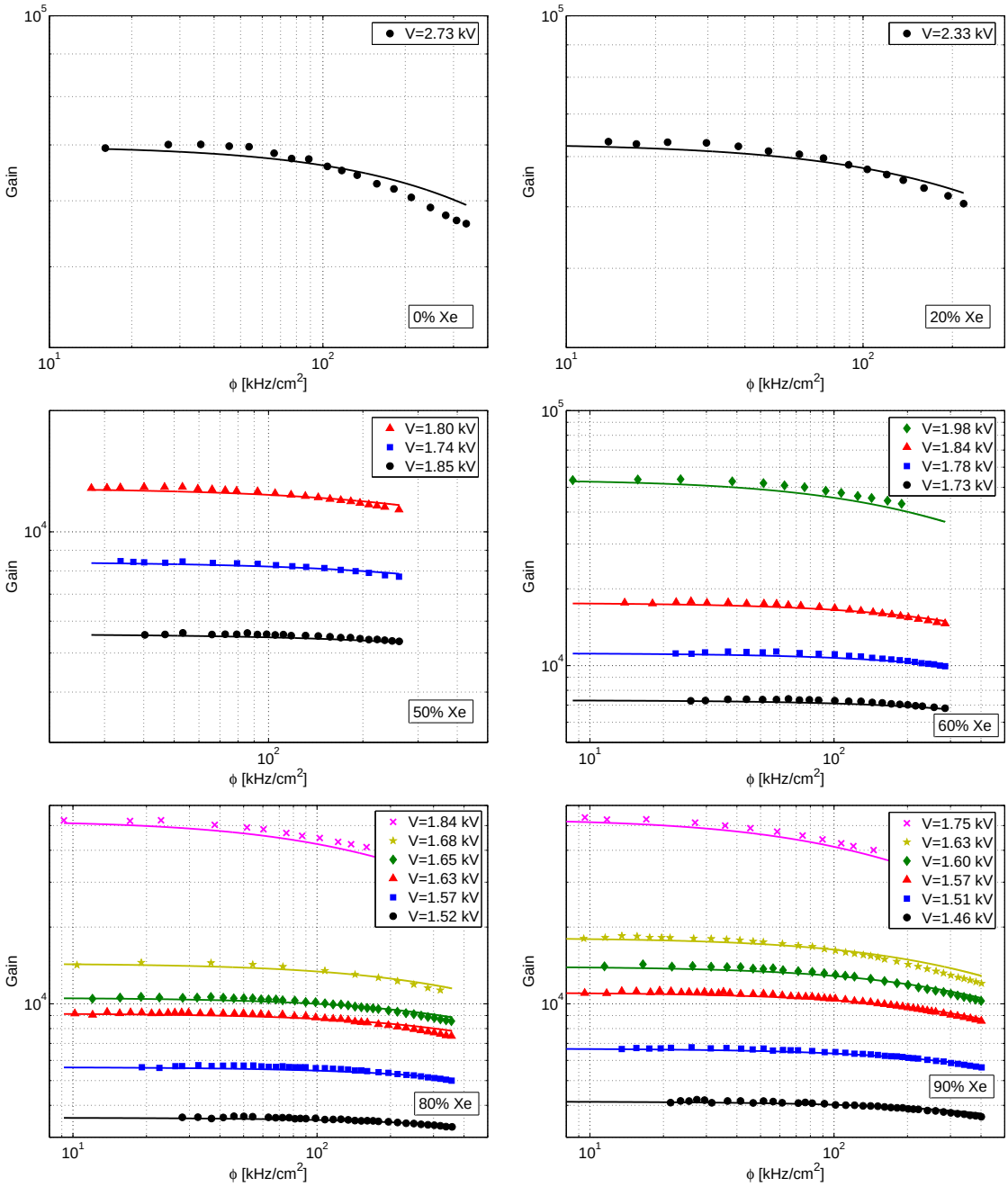


Figure 13. Up-left: 2-parameter fit of the rate curves for Xe-CO_2 mixtures obtained with the $s = 4$ mm chamber.

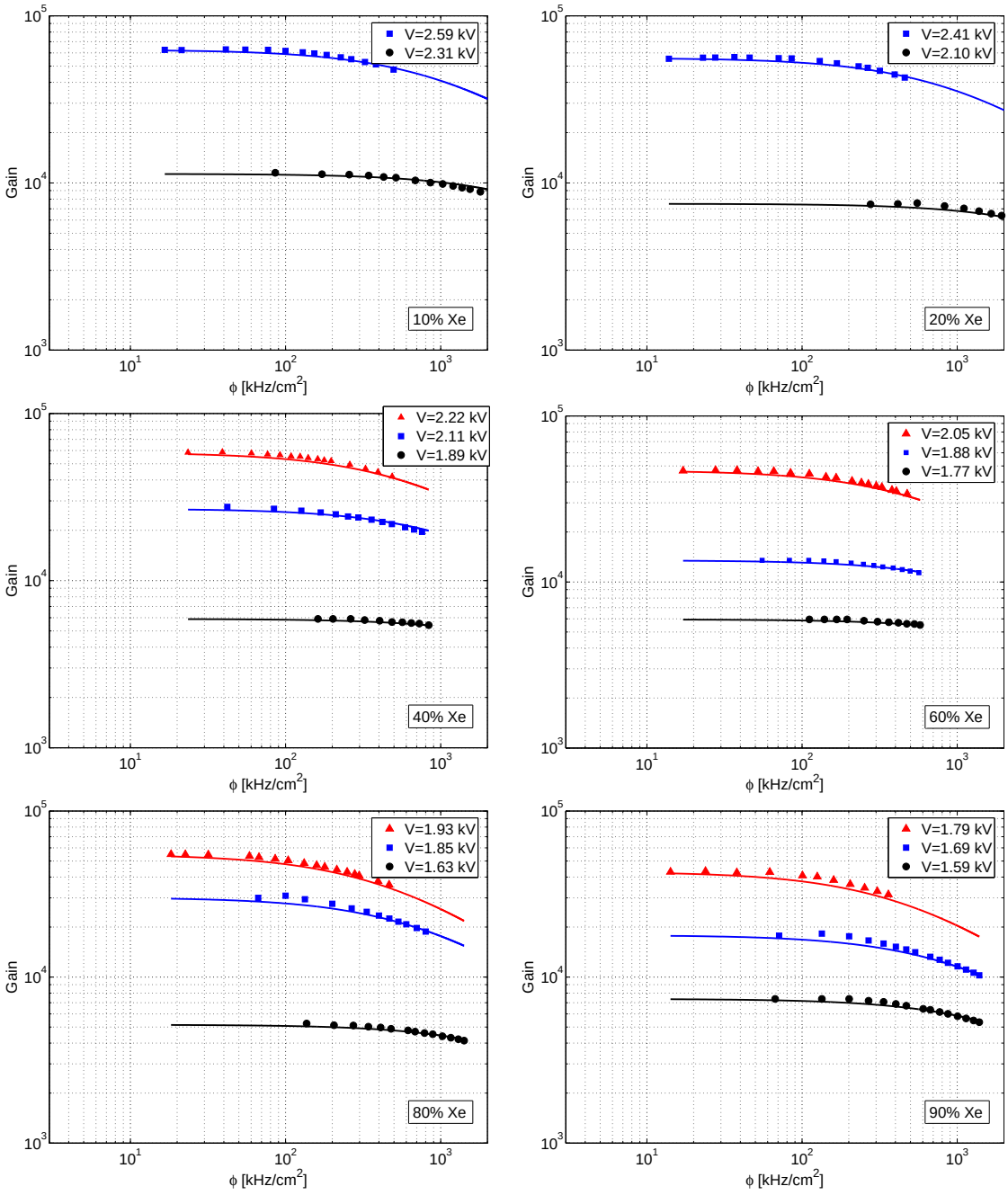


Figure 14. Up-left: 2-parameter fit of the rate curves for Xe-CO_2 mixtures obtained with the $s = 3$ mm chamber.

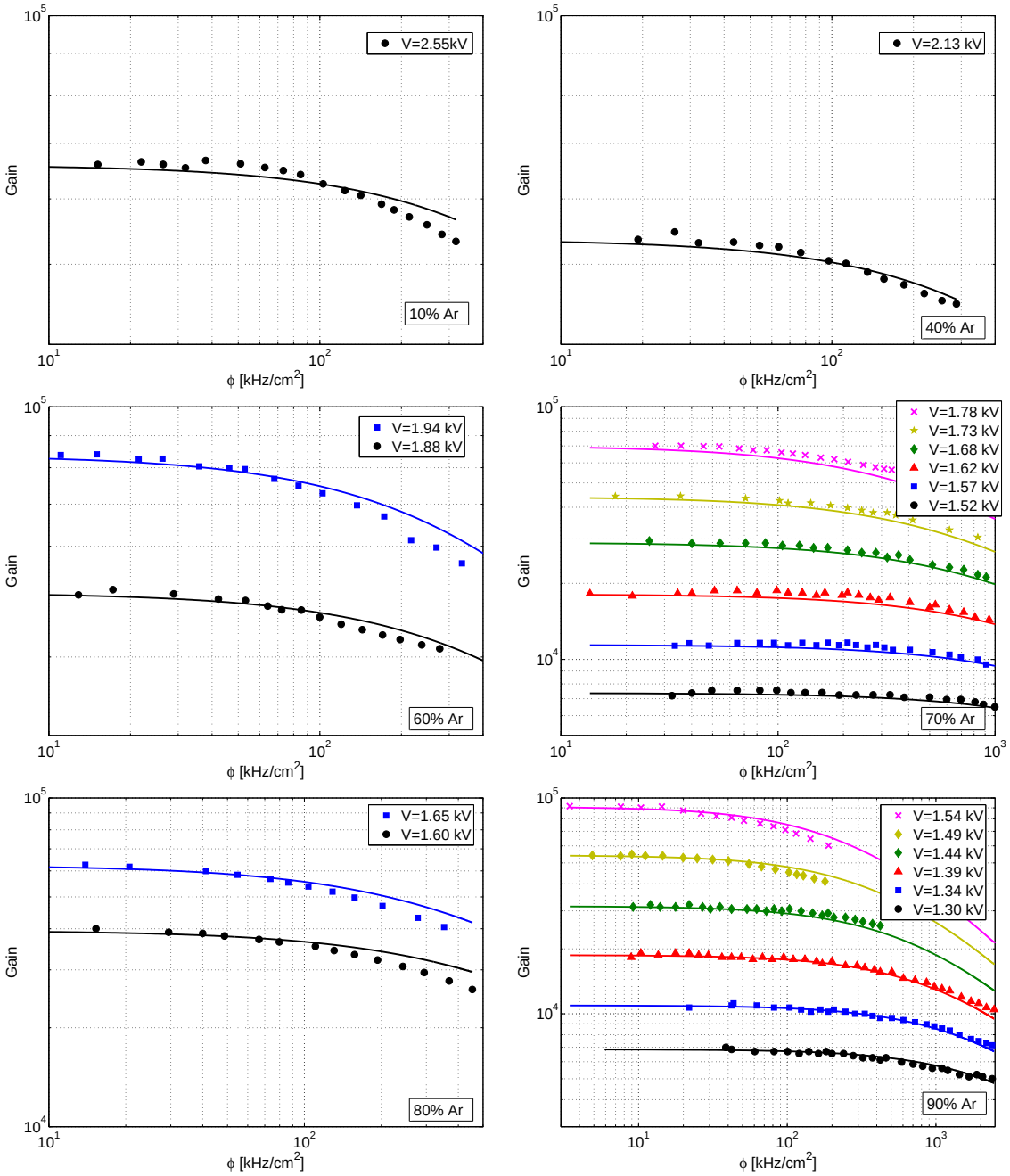


Figure 15. Up-left: 2-parameter fit of the rate curves for Ar-CO_2 mixtures obtained with the $s = 4$ mm chamber.

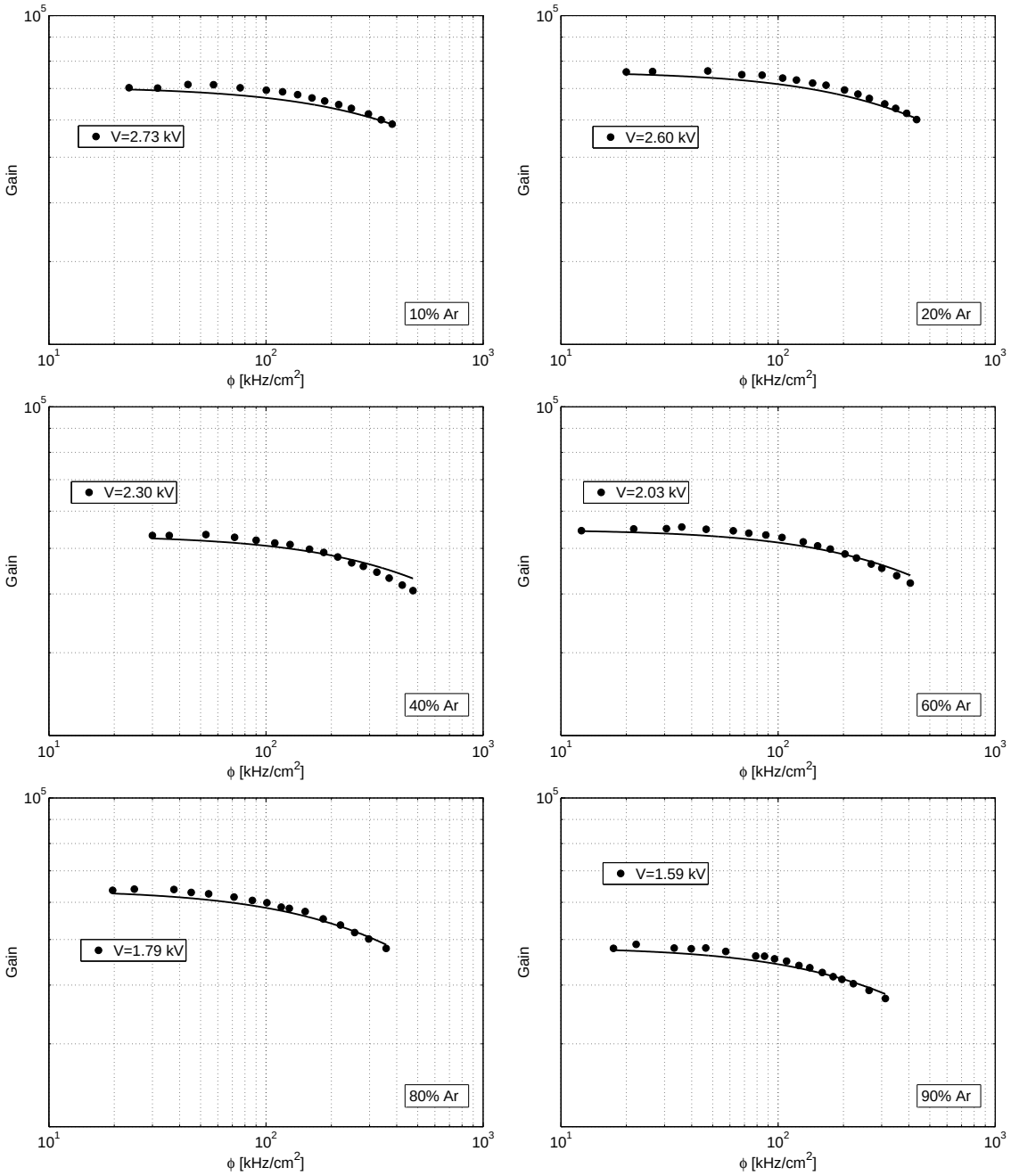


Figure 16. Up-left: 2-parameter fit of the rate curves for Ar-CO_2 mixtures obtained with the $s = 3$ mm chamber.

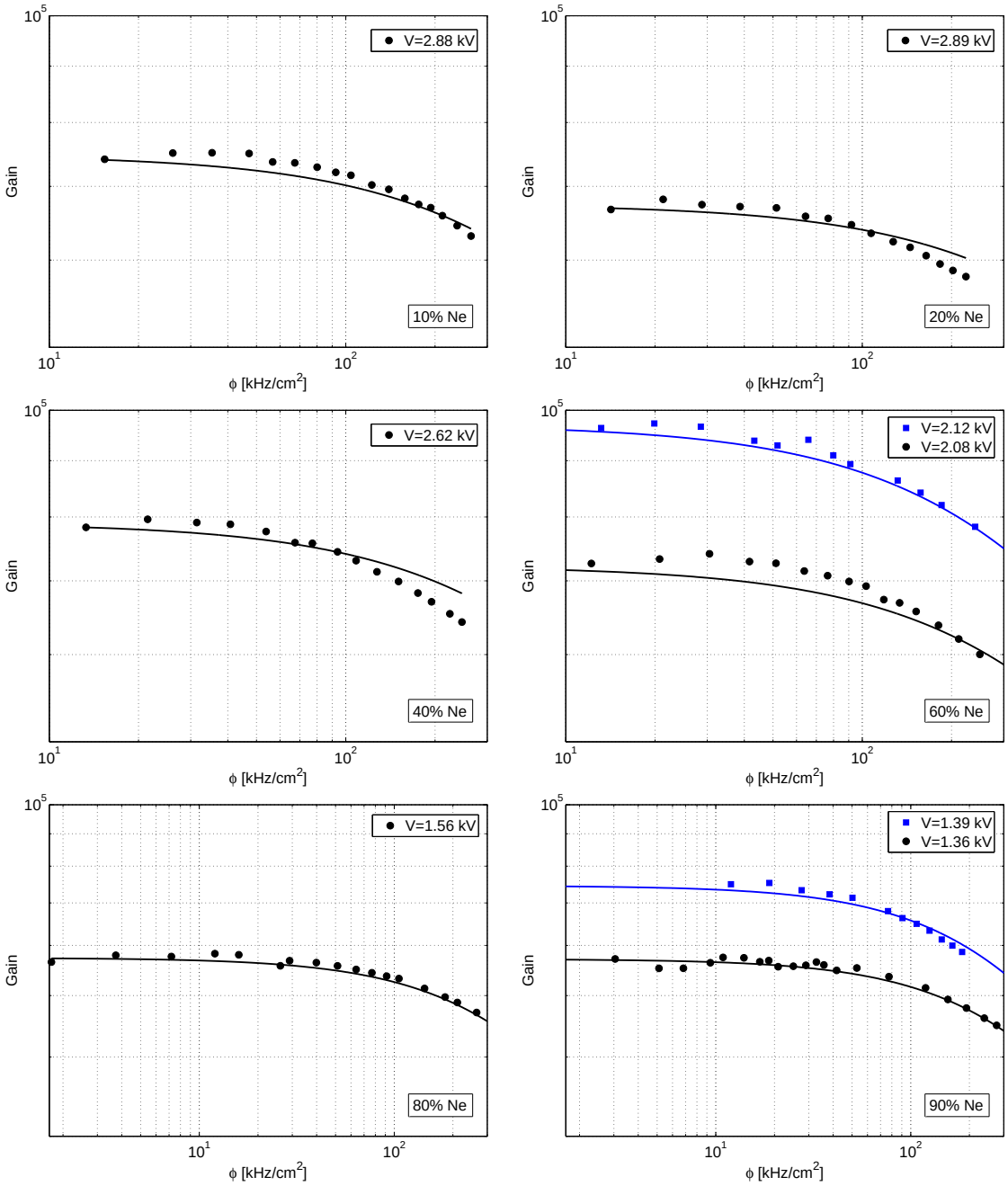


Figure 17. Up-left: 2-parameter fit of the rate curves for Ne-CO_2 mixtures obtained with the $s = 4$ mm chamber.

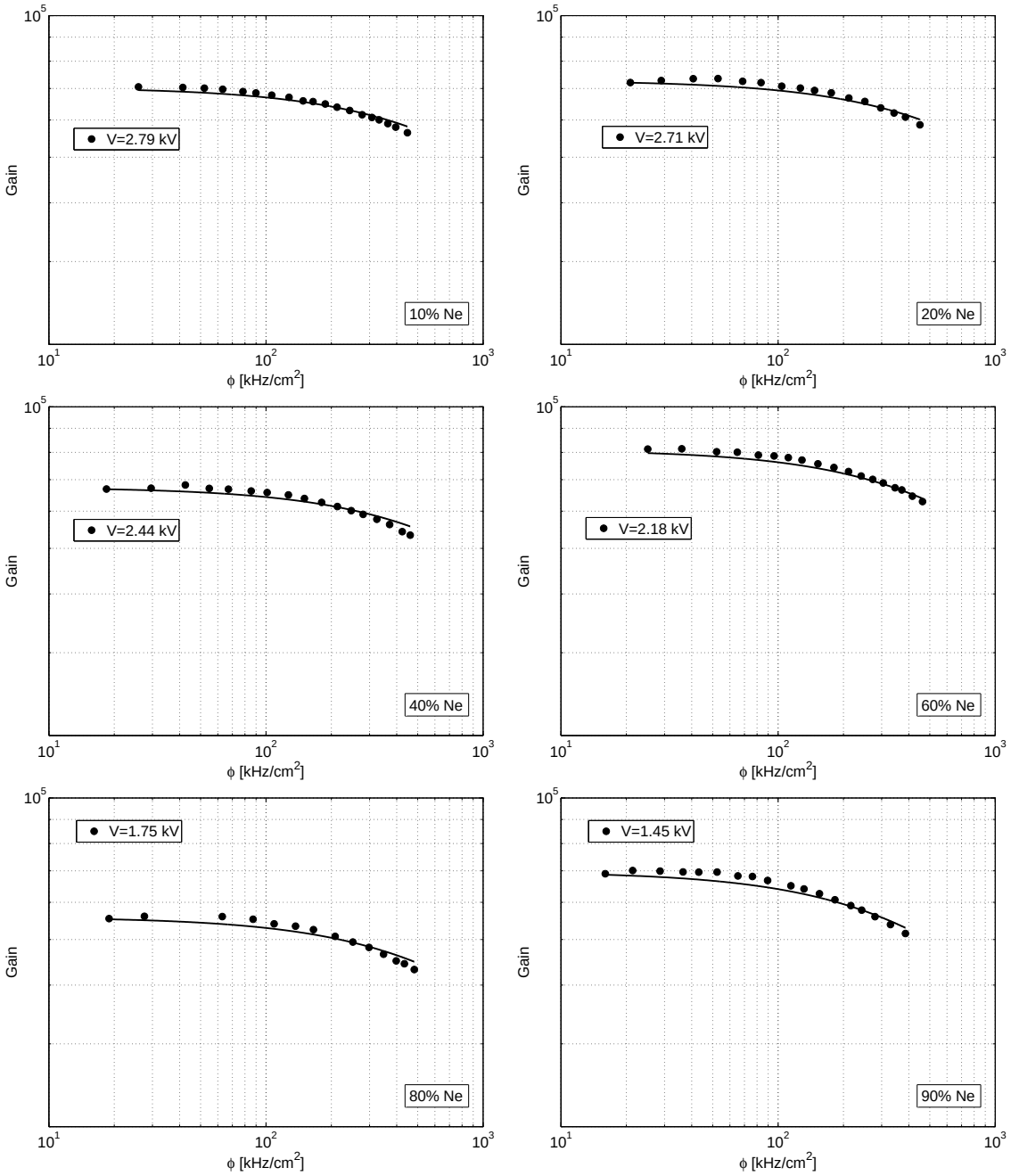


Figure 18. Up-left: 2-parameter fit of the rate curves for Ne-CO_2 mixtures obtained with the $s = 3$ mm chamber.

References

[1] C. Garabatos, Nucl. Instr. and Meth. A, 535(2004)197.

[2] A. Kachtchouk et al., Nucl. Instr. and Meth. A, 555(2005)48.

[3] M. Boehmer, R. Gernhauser et al., Nucl. Instr. and Meth. A, 471(2001)25.

[4] A. Andronic et al., Nucl. Instr. and Meth. A, 558(2006)516.

[5] CBM Technical Status Report, Jan 2005.

[6] A. Andronic, Nucl. Instr. and Meth. A, 563(2006)349.

[7] M. Klein-Bosing et al., Nucl. Instr. and Meth. A, 585(2008)83.

[8] P. Braun-Munzinger and J. Stachel, Nature, 448(2007)302.

[9] A. Andronic et al., Phys.Lett. B, 652(2007)259.

[10] E. Mathieson, Nucl. Instr. and Meth. A, 249(1986)413.

[11] E. Mathieson, G. C. Smith, Nucl. Instr. and Meth. A, 316(1992)246.

[12] F. Sauli, “Principles of operation of multiwire proportional and drift chambers”, CERN-77-09, 1977.

[13] G. Schultz, G. Charpak, F. Sauli, Rev. Phys. App., 12(1977)67.

[14] G. C. Smith, E. Mathieson, IEEE Trans. Nucl. Science. 34-1(1987)411.

[15] W. Riegler, C. Lippmann, B. Schnizer, Nucl. Instr. and Meth. A, 582(2007)469.

[16] H. W. Ellis, R. Y. Pai and E. W. McDaniel, ‘Atomic Data and Nuclear Data Tables’ 17(1976)177.

[17] M. Petris et al., Nucl. Instr. and Meth. A, 581(2007)406.

[18] A. Andronic et al. Nucl. Instr. and Meth., 519(2004)508.

[19] S M. Seltzer, M. J. Berger, Int. J. Appl. Radiat. Isot. Vol. 35, 7(1984)665.

[20] E. Basurto, J. de Urquijo, I. Alvarez, C. Cisneros, Phys. Rev. E 61, 3(2000)305.